Article ID: 1000-324X(2022)10-1141-08 **DOI:** 10.15541/jim20220033

NiN_4/Cr Embedded Graphene for Electrochemical Nitrogen Fixation

WU Jing[1], YU Libing[1], LIU Shuaishuai[1], HUANG Qiuyan[1], JIANG Shanshan[1], ANTON Matveev[2], WANG Lianli[3], SONG Erhong[4], XIAO Beibei[1]

(1. School of Energy and Power Engineering, Jiangsu University of Science and Technology, Zhenjiang 212003, China; 2. National Research Ogarev Mordovia State University, Saransk 430005, Russia; 3. School of Materials Science and Engineering, Xi'an University of Science and Technology, Xi'an 710054, China; 4. State Key Laboratory of High Performance Ceramics and Superfine Microstructure, Shanghai Institute of Ceramics, Chinese Academy of Sciences, Shanghai 200050, China)

Abstract: Owing to the heavy energy consumption and the massive CO_2 emission during ammonia synthesis *via* Haber-Bosch process, a clean technology of nitrogen reduction electrocatalysis under ambient conditions is of significance for the sustainable energy conversion progress in future. In the study, the nitrogen reduction reaction of TM_1N_4/TM_2 embedded graphene is comprehensively investigated using density functional theory calculations. Fully considering the activity and stability, our results reveal that NiN_4/Cr anchored graphene exhibits the best catalytic activity *via* the enzymatic reaction pathway wherein the potential determining step is located at the first hydrogenation with an onset potential of 0.57 V, being superior to the commercial Ru-based material. Furthermore, compared with the isolated Cr atom decorated nitrogen functionalized graphene, the introduction of NiN_4 moiety decreases ΔG_{max} and enhances the electrocatalytic performance. According to the Mulliken charge analysis, the physical origin of the catalytic activity is ascribed to the electron transition between the supports and reaction intermediates. Overall, these results pave a way for the design of the high efficient electrode material for ammonia synthesis and provide a fundamental insight into the electrocatalysis.

Key words: nitrogen reduction reaction; graphene; density functional theory; electrocatalysis; thermodynamics

Ammonia is an important chemical material that is widely used in industrial and agricultural production[1-5]. Currently, ammonia is mainly produced *via* the Haber-Bosch process in industry by using nitrogen and hydrogen as raw materials[6-9]. In order to break the inherent inert N≡N triple bond, the Haber-Bosch process using Fe and Ru metal-based catalysts with promoters under the harsh reaction environment, leading to the heavy energy consumption and the massive CO_2 emission[10-13]. Naturally, ammonia synthesis *via* nitrogen reduction reaction under mild conditions becomes an economic and eco-friendly way, which is inspired by the soybean rhizobium and bacteria nitrogenase[14]. Based on this strategy, exploring efficient catalysts that can effectively facilitate electrochemical nitrogen reduction reaction (NRR) is desirable, however, it remains a big challenge.

Graphene has shown attractive catalytic activity due to its extraordinary electronic, thermal and mechanical properties[15]. Considering its electron neutrality, the common strategy to activate the inert graphene is the direct introduction of the TM/N heteroatoms as the active sites. For example, Choi *et al*.[4] have reported that several single atom catalysts (SACs) including TiN_4 and VN_4 embedded graphene exhibits better activity in comparison with Ru (0001) stepped surface. Furthermore, Yang *et al*.[16] have reported that among varied TMN_4 embedded graphene (TM = Fe, Co, Mo, W, Ru, Rh), the MoN_4 site exhibits outstanding catalytic activity for ammonia synthesis with small reaction energy barrier of 0.67 eV. Analogously, Riyaz *et al.*[17] have demonstrated that the best activity is offered by CrN_4 site among

Received date: 2022-01-20; **Revised date:** 2022-04-06; **Published online:** 2022-05-09
Foundation item: National Natural Science Foundation of China (21503097); Natural Science Foundation of Shaanxi Province (2018JQ5181); Science and Technology Commission of Shanghai Municipality (21ZR1472900)
Biography: WU Jing(1998–), female, Master candidate. E-mail: wjjust20@163.com
吴 静(1998–), 女, 硕士研究生. E-mail: wjjust20@163.com
Corresponding author: XIAO Beibei, associate professor. E-mail: xiaobb11@mails.jlu.edu.cn;
SONG Erhong, associate professor. E-mail: ehsong@mail.sic.ac.cn
肖蓓蓓, 副教授. E-mail: xiaobb11@mails.jlu.edu.cn; 宋二红, 副研究员. E-mail: ehsong@mail.sic.ac.cn

different TMN_4 (TM=Cr, Mn, Fe, Mo, Ru) embedded graphene.

Compared with single-metal atom catalysts, double atom catalysts (DACs) with synergetic interatomic interactions and flexible active sites, can maximize the potentials of catalysts, which makes the optimization of activity and selectivity feasible. They have emerged as more beneficial catalysts for electrochemical reactions. For instance, Sun *et al*.[18] have revealed that VFe-N-C shows the best catalytic activity for electrochemical NRR with limiting potential of –0.36 V. Analogously, Zheng *et al*.[19] have reported that only Fe/Mn-N-C catalyst is identified to be a promising candidate for NRR. The fascinating activity modification motivates our interest on the NRR reactivity catalyzed by DACs. Interestingly, Zhou *et al*.[20] have successfully introduced the secondary Rh atom into the FeN_4 pre-embedded graphene experimentally and the obtained FeN_4/Rh sample delivers the superior electrocatalytic activity. Therefore, we are interested in the N_2-to-NH_3 performance of TM_1N_4/TM_2 combination induced by the introduction of the second TM heteroatom into the TMN_4 pre-doping graphene. However, it has not been explored yet.

In this study, the NRR performance of the TM_1N_4/TM_2 embedded graphene is systematically investigated by density function theory calculations. According to our results, the NiN_4/Cr combination is a potential electrocatalyst for the N_2-to-NH_3 conversion. Besides, the Mulliken charge analysis identifies the electron transfer between the functional graphene and the NRR intermediates. The presented results provide a theoretical guide for the catalyst synthesis experimentally.

1 Computational method

All calculations are performed within the density functional theory (DFT) framework as implemented in $DMol^3$ code[21-22]. The generalized gradient approximation (GGA) with the Perdew-Burke-Ernzerhof (PBE) functional is employed to describe exchange-correlation interactions[23]. The DFT Semi-core Pseudopotential (DSPP) core treat method is implemented for relativistic effects, which replaces core electrons by a single effective potential and introduces some degree of relativistic corrections into the core[24]. The double numerical atomic orbital augmented by a polarization function (DNP) is chosen as the basis set[21]. A smearing of 0.005 Ha (1 Ha=27.21 eV) to the orbital occupation is applied to achieve accurate electronic convergence. In the geometry structural optimization, the convergence tolerances of energy, maximum force and displacement are 1.0×10^{-5} Ha, 0.02 Ha/nm and 0.0005 nm, respectively. The spin-unrestricted method is used for all calculations. A conductor-like screening model (COSMO) was used to simulate a H_2O solvent environment for all calculations[25]. COSMO is a continuum model in which the solute molecule forms a cavity within the dielectric continuum. The $DMol^3$/COSMO method has been generalized to periodic boundary cases. The dielectric constant is set as 78.54 for H_2O. During the geometrical optimization, the systems are free to relax.

The 4×4 supercell is an appropriate choice in the consideration of avoiding the interaction among images and reducing the cumbersome calculation[26-29]. The 2 nm-thick vacuum is added to avoid the artificial interactions between the catalyst and its images in the *Z* direction. The adsorption energies (E_{ads}) of NRR intermediates are calculated by

$$E_{ads}=E_{system}-E_{catalyst}-E_m \quad (1)$$

where E_{system}, $E_{catalyst}$ and E_m represent the total energy of the adsorption system, the catalyst and the adsorbates, respectively.

Six proton-electron transfer steps were involved in the electrochemical NH_3 synthesis from N_2, *i.e.*, $N_2+6H^++6e^-\rightarrow2NH_3$. Gibbs free energy change (ΔG) of each elementary step was computed by computational hydrogen electrode model (CHE) raised by Nørskov *et al.*, which the chemical potential of (H^++e^-) pairs equaled to one-half of H_2 at standard condition[30-31]. The ΔG was determined by

$$\Delta G=\Delta E+\Delta ZPE-T\Delta S+\Delta G_U+\Delta G_{pH} \quad (2)$$

where ΔE is the reaction energy analyzed directly from the DFT computations, ΔZPE and ΔS are the zero point-energy and the entropy difference at room temperature (T=298.15 K), respectively. The zero-point energies and entropies of the NRR intermediates are calculated from the vibrational frequencies according to standard methods. Following the suggestion of Wilcox, *et al.*[32], the substrates are fully constrained for the frequency calculation. The term of $\Delta G_U=-eU$ corresponds to the free energy contribution caused by the variation of electrode potential. ΔG_{pH} is the pH correction of the free energy, which could be expressed as $\Delta G_{pH}=2.303\times k_BT\times pH$, where k_B is the Boltzmann constant and pH is set to zero. $\Delta G<0$ corresponds to an exothermic adsorption process *vice versa*. Furthermore, the onset potential was defined as the applied potential (U) required such that every step in the specified mechanism is exergonic.

2 Results and discussion

The atomic structure is illustrated in Fig.1(a). TM_1 denotes the TM atom in TMN_4 moiety and TM_2 is the secondary dopant wherein TM_1 considers Mn, Fe, Co and

Ni elements according to the experimental accessibility and TM_2 screens 3d/4d/5d TM elements[20,33-34]. For simplicity, the TM_1N_4/TM_2 embedded graphene is referred as TM_1N_4/TM_2. Fig. 1 (b) provides the screening criterion. In order to reduce the cumbersome calculations, the competition between NRR and the side hydrogen evolution reaction (HER) is firstly considered *via* comparing the strengths of the adsorption energies E_{ads}. Herein, $E_{ads}(N_2)$ is greater than $E_{ads}(H)$, indicating the favorable nitrogen adsorption. The preferential N_2 adsorption could suppress the adverse HER and boost the electrochemical NH_3 synthesis[8]. Subsequently, in order to ensure the activation of N_2 molecule, the $E_{ads}(N_2)$ should be stronger than –0.6 eV[35]. Herein, the three-coordination TM_2 site is identified as the active site. The strong adsorption ability originates from the donation-back-donation mechanism that accepting the lone-pair electrons of N_2 with the empty orbitals of TM site and thereby donating the

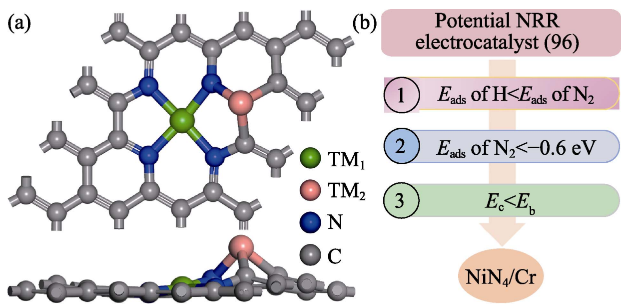

Fig. 1　(a) Atomic structure of TM_1N_4/TM_2 and (b) screening criterion for TM_1N_4/TM_2 combination

occupied orbital electrons into the antibonding orbitals of N_2. The data of $E_{ads}(N_2)$ and $E_{ads}(H)$ are listed in Table S1-S4 in the supporting materials for clear reference. According to the mentioned consideration, there are total 55 combinations identified.

According to literature data, the potential determining step (PDS) of NRR is usually located at the first protonation process, the formation of NNH[35-36]. For a quick screening, the free energy of the NNH formation ($\Delta G_{N2\text{-}NNH}$) is evaluated in priority. The data are presented in Fig.2 where the $\Delta G_{N2\text{-}NNH}$ value of the commercial Ru is added as reference since it is the optimal pure metal catalyst for the industrial process[37]. Therein, the most exergonic step in the reduction to form ammonia on Ru(0001) is the addition of the first hydrogen atom to form NNH and the step is 1.08 eV uphill in free energy[37].

According to the results, we focus our attention on the systems with relatively low $\Delta G_{N2\text{-}NNH}$, including MnN_4/W, MnN_4/Re, FeN_4/W, FeN_4/Re, CoN_4/Re, NiN_4/Cr, NiN_4/Mo, NiN_4/Ta, NiN_4/W and NiN_4/Re. Noteworthy, it is necessary to test the stability of materials against the agglomeration of dispersible metal atoms. The thermodynamic stability of atomic distribution is evaluated *via* the binding energy E_b[38]. Fig. S1 in the supporting materials reveals that E_b of NiN_4/Cr, NiN_4/Mo and NiN_4/Ta exceed the corresponding cohesive energy E_c, indicating the good resistance against clustering. According to the mentioned discussion, the potential electrode materials are identified as NiN_4/Cr, NiN_4/Mo and NiN_4/Ta. Therefore, we perform the complete free energy profiles of the

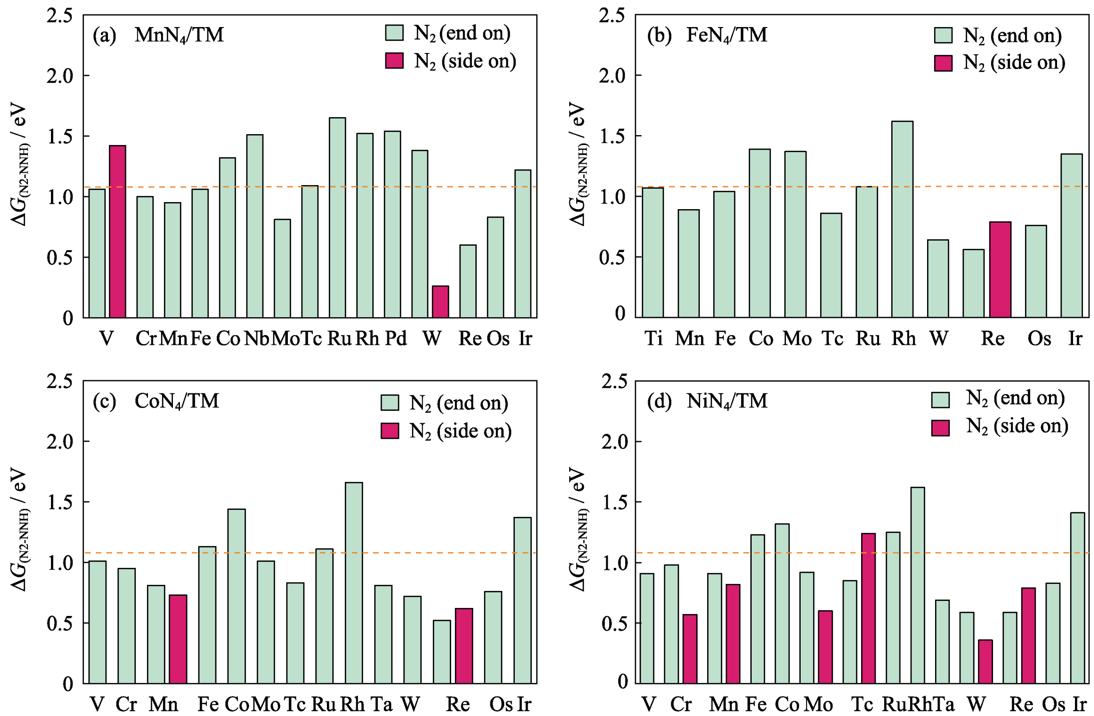

Fig. 2　Gibbs free energy difference between N_2 and NNH with the orange line at 1.08 eV

Colorful figures are available on website

NRR progress focused on the three candidates in the following discussion.

Fig. 3 shows the reaction mechanisms including distal, alternating and enzymatic mechanisms[35,39-40]. The end-on adsorption of nitrogen molecule prefers a distal or alternating mechanism. In distal mechanism, the pair of electrons continuously attacks the nitrogen atom farthest from the catalyst's surface, releasing an ammonia molecule, which then attacks a second nitrogen atom to form another ammonia molecule. In alternating mechanism, the hydrogenation step alternates between two nitrogen atoms on the surface of the catalyst. Nitrogen molecules adsorbed by side-on manner can be reduced to ammonia by enzymatic mechanism, in which two nitrogen atoms alternately hydrogenated on the catalyst surface by proton-electron pairs and release the first ammonia molecule, thereby forming the second one. The free energy changes Δ*G* of the elementary steps of NiN_4/Cr, NiN_4/Mo and NiN_4/Ta are summarized in Table S5 in the supporting materials.

Fig. 4 gives the free energy profile of NiN_4/Cr combination as an illustration. Wherein, the free energy of the $*N_2$ end-on adsorption is downhill by 0.41 eV indicating its spontaneity. In distal mechanism, the free energy of the *N–NH formation is uphill by 0.98 eV. In the second protonation step, the exothermic character of $*N–NH_2$ formation is observed with the Δ*G* of –0.28 eV. Subsequently, the release of the first NH_3 requires overcoming 0.17 eV of energy. The second $*NH_3$ is formed by the *N consecutive reduction where *NH, $*NH_2$ and $*NH_3$ formation is downhill trend with the Δ*G* of –1.08, –1.09 and –0.23 eV. Finally, desorption of the second $*NH_3$ is hindered by the endothermic Δ*G* of 1.04 eV. Noteworthy, NH_4^+ reacted from $*NH_3$ protonation would be desorbed easily with aid of the solution[4]. Therefore, the elementary step of the $*NH_3$ desorption is not a problematic obstacle in NRR[41]. Herein, the PDS in the distal pathway is located at the first protonation with the ΔG_{max} of 0.98 eV. Analogously, Δ*G* of the first protonation step *via* the alternating mechanism is uphill by 0.98 eV. In the second protonation step, the endothermic character of *NH–NH formation is observed with the Δ*G* of 0.05 eV, indicating the stability of *N–NH structure. Later, an exothermic trend was found in the following protonation, with Δ*G* values of –0.31, –0.25, –1.29 and –0.71 eV, respectively. Herein, the PDS is also identified at the first protonation for the alternating mechanism with the same ΔG_{max} of 0.98 eV. Furthermore, for enzymatic mechanism, the free energy of the $*N_2$ side-on adsorption decreased by 0.10 eV. Subsequently, the formation of *N–*NH and *NH–*NH requires overcoming 0.57 and 0.16 eV of energy. In the following protonation process, the downhill trends are revealed by the corresponding Δ*G* of –0.56, –0.12, –1.51 and –0.38 eV, respectively. Herein, the PDS is located at the first protonation of *N–*NH formation with the value of 0.57 eV. In order to overcome the thermodynamic barrier, the applied *U* is shifted to 0.98, 0.98 and 0.57 V for distal, alternating and enzymatic mechanism, respectively. The lower onset potential corresponds to the better activity. Therefore, the preferred mechanism of NRR on NiN_4/Cr is the enzymatic pathway. Herein, it is noteworthy that our discussion is based on the abundant proton in the acid solution. However, the efficiency of aqueous NRR is complicatedly dependent on the proton supply. The proton-poor neutral/alkaline solutions are generally used to lower the proton accessibility for a suppressed HER in order to improve the NRR efficiency. On the other hand, the limited proton from water splitting also deteriorates NH_3 formation since NRR is essentially related to the hydrogenation reactions. Therefore, the variation of the NRR performance caused by different pH solution is still under the debate[42-44].

The free energy profiles of NiN_4/Mo and NiN_4/Ta are presented in Fig. S2 and Fig. S3 in the supporting materials, respectively. As for the former, the PDS are preserved at the first protonation step with the ΔG_{max} of 0.92, 0.92 and 0.60 eV, respectively. Therefore, NRR

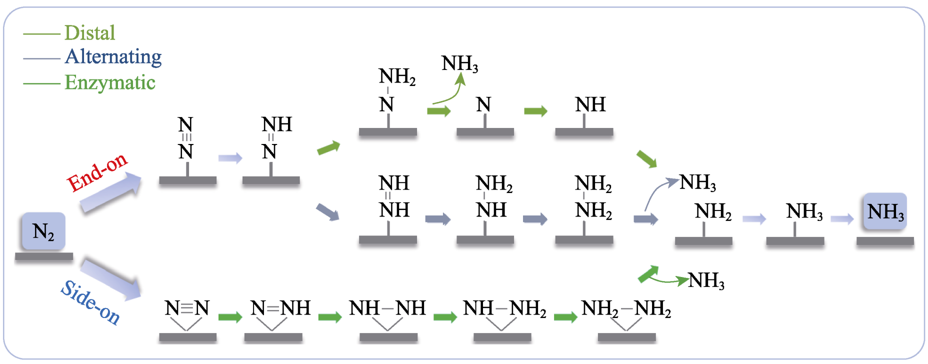

Fig. 3 Schematic reaction mechanisms
Colorful figure is available on website

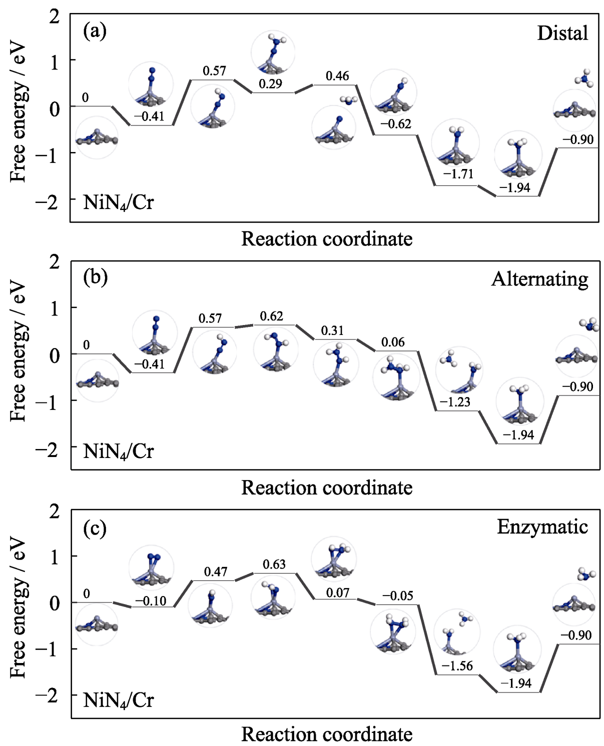

Fig. 4　Free energy diagrams and the corresponding configuration of the NRR intermediates on NiN_4/Cr

NRR mechanisms are (a) distal, (b) alternating and (c) enzymatic

follows the enzymatic pathway on NiN_4/Mo with the overpotential of 0.60 V. As for the latter, the PDS is the first protonation step for the distal and alternating pathway and the ΔG_{max} of 0.69 eV, meanwhile the high ΔG_{max} is located at the $*NH_2$–$*NH_2$ formation with the value of 0.58 eV for the enzymatic pathway. However, the enzymatic pathway of NiN_4/Ta is unfavorable considering the endothermic character of the *N–*N adsorption. Therefore, the preferred mechanism of NRR on NiN_4/Ta is the distal or alternating. According to the above analysis, ΔG_{max} is ordered by NiN_4/Cr (0.57 eV)<NiN_4/Mo (0.60 eV) < NiN_4/Ta (0.69 eV). Therefore, the mentioned candidates show outstanding activities, being promising alternatives to the commercial Ru(0001)[37]. Furthermore, the potential determining step and the free energy change ΔG_{max} are summarized in Table S6. We further add the data of Cr/Mo/Ta embedded nitrogen functionalized graphene, which are from the free energy profiles in Fig. S4–S6. In comparison with Cr single- atom catalyst, NiN_4/Cr decreases the ΔG_{max} from 0.66 to 0.57 eV, indicating a boosted activity caused by synergetic interatomic interactions. In contrast, the combination of NiN_4/Mo as well as NiN_4/Ta inversely deteriorates the NRR efficiency due to the increased ΔG_{max}. Therefore, NiN_4/Cr is a promising candidate for experimental synthesis.

In order to further reveal the catalytic effect, the Mulliken charge analysis was performed. In line with previous reports[40,45-47], there are three moieties, including moiety 1 (the graphene substrate), moiety 2 (active center) and moiety 3 (NRR intermediates). Fig. 5 presents the

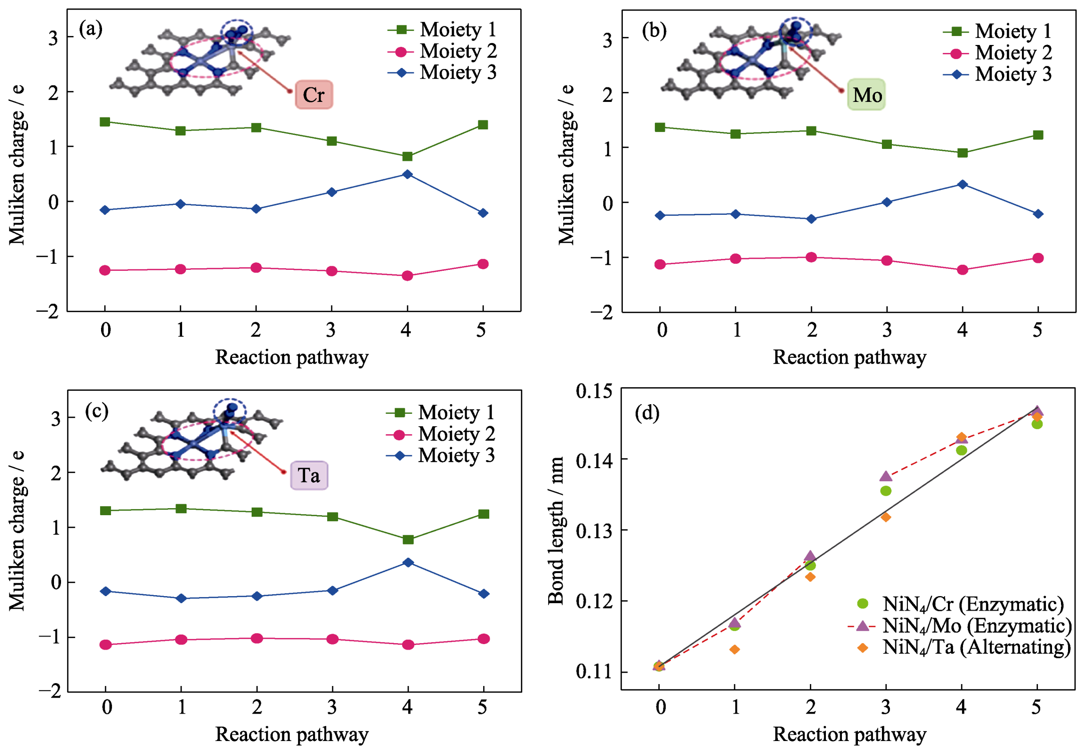

Fig. 5　(a-c) Charge variation of the three moieties along the optimal pathway and (d) N–N bond length change in NRR along preferred pathway

Moieties 1, 2, 3 represent the graphene substrate, active center, and NRR intermediates, respectively charge variation of NiN_4/Cr, NiN_4/Mo and NiN_4/Ta during the protonation steps. The charge transfer is observed between the adsorbent and the substrate, in consistent with previous reports[45]. Besides, Fig. 5(d) monitors the N–N bond lengths of the NRR intermediates. Therein, the stretch of N–N bond is obvious, indicating that the protonation continuously activates the inert N–N bonds and leads to the energetic feasibility of the N_2-to-NH_3 conversion under the mild condition.

In the end, it is noteworthy that the N vacancy would be created during the reduction environment and act as the active site, besides the transition metal site discussed above. Herein, we further consider the role of nitrogen vacancy. Fig. S7 in the supporting materials presents the corresponding free energy profiles of N_2-to-NH_3 conversion. For convenience, four different N vacancies are donated as 1N, 2N, 3N and 4N, respectively. The results reveal that the 1N and 2N sites are unable to capture N_2 molecule due to the endothermic character meanwhile the first protonation on the 4N site is energetically limited. Differently, the free energy profile of 3N site is continuously declined, demonstrating its feasibility to boost N_2-to-NH_3 conversion. Therefore, the 3N vacancy would act as an active site for ammonia synthesis. However, according to the reaction of $N_4^*+3(H^++e^-)\rightarrow N_3^*+NH_3$, the formation energy of 3N site is 3.70 eV. It is energy-demanding process, implying the difficulty for the vacancy formation. It stems from the strong interaction between N atom and its surrounding, as reflected by the binding energy with the value of 9.91 eV. Furthermore, Fig. S8 in the supporting materials reveals that the nitrogen atom is accessible for one hydrogen atom but it is unable to capture more hydrogen atoms. Therefore, the creation of the N vacancy *via* protonation steps is energetically adverse. Considering the mentioned discussion, we do not further devote our attention on the N vacancy.

3 Conclusions

In summary, the NRR performance of the TM_1N_4/TM_2 embedded graphene is systematically investigated by means of density functional theory calculation. Considering activity and stability, our results reveal that NiN_4/Cr, NiN_4/Mo and NiN_4/Ta exhibit outstanding performance toward NRR, being promising alternatives to the commercial Ru(0001). Herein, ΔG_{max} is ordered by NiN_4/Cr (0.57 eV)<NiN_4/Mo (0.60 eV)<NiN_4/Ta (0.69 eV). Besides, the Mulliken charges analysis certifies that the activation of the NRR intermediates is ascribed to the electron transfer between the graphene substrate and NRR intermediates. This study provides the potential graphene-based nanomaterial for electrocatalytic synthesis of ammonia.

Supporting materials

Supporting materials related to this article can be found at https://doi.org/10.15541/jim20220033.

References:

[1] WANG Y, JIA K, PAN Q, *et al*. Boron-doped TiO_2 for efficient electrocatalytic N_2 fixation to NH_3 at ambient conditions. *ACS Sustain. Chem. Engineer.*, 2018, **7(1):** 117–122.

[2] LI H Y, YANG L, WANG Z X, *et al*. N-heterocyclic carbene as a promising metal-free electrocatalyst with high efficiency for nitrogen reduction to ammonia. *J. Energy Chem.*, 2020, **46(7):** 78–86.

[3] LI Q Y, HE L Z, SUN C H, *et al*. Computational study of MoN_2 monolayer as electrochemical catalysts for nitrogen reduction. *J. Phys. Chem. C*, 2017, **121(49):** 27563–27568.

[4] CHOI C, BACK S, KIM N Y, *et al*. Suppression of hydrogen evolution reaction in electrochemical N_2 reduction using single-atom catalysts: a computational guideline. *ACS Catal.*, 2018, **8(8):** 7517–7525.

[5] ZHAO W H, ZHANG L F, LUO Q Q, *et al*. Single $Mo_1(Cr_1)$ atom on nitrogen-doped graphene enables highly selective electroreduction of nitrogen into ammonia. *ACS Catal.*, 2019, **9(4):** 3419–3425.

[6] WANG S Y, SHI L, BAI X W, *et al*. Highly efficient photo-/ electrocatalytic reduction of nitrogen into ammonia by dual-metal sites. *ACS Central Sci.*, 2020, **6(10):** 1762–1771.

[7] MA B Y, PENG Y, Ma D W, *et al*. Boron-doped InSe monolayer as a promising electrocatalyst for nitrogen reduction into ammonia at ambient conditions. *Appl. Surf. Sci.*, 2019, **495(30):** 143463.

[8] LING C Y, NIU X H, LI Q, *et al*. Metal-free single atom catalyst for N_2 fixation driven by visible light. *J. Am. Chem. Soc.*, 2018, **140(43):** 14161–14168.

[9] LIU X, WANG Z X, ZHAO J, *et al*. Two-dimensional π-conjugated osmium bis(dithiolene) complex (OsC_4S_4) as a promising electrocatalyst for ambient nitrogen reduction to ammonia. *Appl. Surf. Sci.*, 2019, **487(1):** 833–839.

[10] JI S, WANG Z X, ZHAO J X, A boron-interstitial doped C_2N layer as a metal-free electrocatalyst for N_2 fixation: a computational study. *J. Mater. Chem. A*, 2019, **7(5):** 2392–2399.

[11] ZHANG X, CHEN A, ZHANG Z H, *et al*. Double-atom catalysts: transition metal dimer-anchored C_2N monolayers as N_2 fixation electrocatalysts. *J. Mater. Chem. A*, 2018, **6(38):** 18599–18604.

[12] LI F F, CHEN L, LIU H M, *et al*. Enhanced N_2-fixation by engineering the edges of two-dimensional transition-metal disulfides. *J. Phys. Chem. C*, 2019, **123(36):** 22221–22227.

[13] QIN G Q, CUI Q Y, DU A J, *et al*. Transition metal diborides: a new type of high-performance electrocatalysts for nitrogen reduction. *ChemCatChem*, 2019, **11(11):** 2624–2633.

[14] ZHU H R, HU Y L, WEI S H, *et al*. Single-metal atom anchored on boron monolayer (β_{12}) as an electrocatalyst for nitrogen reduction into ammonia at ambient conditions: a first-principles study. *J. Phys. Chem. C*, 2019, **123(7):** 4274–4281.

[15] WANG S M, ZHANG L, QIN Y, *et al*. Co, N-codoped graphene as efficient electrocatalyst for hydrogen evolution reaction: insight into the active centre. *J. Power Sources*, 2017, **363(30):** 260–268.

[16] YANG Y L, LIU J D, WEI Z X, *et al*. Transition metal-dinitrogen complex embedded graphene for nitrogen reduction reaction. *ChemCatChem*, 2019, **11(12):** 2821–2827.

[17] RIYAZ M, GOEL N, Single-atom catalysis using chromium embedded in divacant graphene for conversion of dinitrogen to ammonia. *ChemPhysChem*, 2019, **20(15):** 1954–1959.

[18] SUN C N, WANG Z L, LANG X Y, *et al*. Synergistic effect of active sites of double-atom catalysts for nitrogen reduction reaction. *ChemSusChem*, 2021, **14(20):** 4593–4600.

[19] ZHENG X N, YAO Y, WANG Y, *et al*. Tuning the electronic structure of transition metals embedded in nitrogen-doped graphene for electrocatalytic nitrogen reduction: a first-principles study. *Nanoscale*, 2020, **12(17):** 9696–9707.

[20] ZHOU Y, SONG E H, CHEN W, *et al*. Dual-metal interbonding as the chemical facilitator for single-atom dispersions. *Adv. Mater.*, 2020, **32(46):** e2003484.

[21] DELLY B. An all-electron numerical method for solving the local density functional for polyatomic molecules. *J. Chem. Phys.*, 1990, **92(1):** 508–517.

[22] DELLY B, From molecules to solids with the $DMol^3$ approach. *J. Chem. Phys.*, 2000, **113(18):** 7756–7764.

[23] OERDEW J P, BURKE K, ERNZERHOF M. Generalized gradient approximation made simple. *Phys. Rev. Lett.*, 1996, **77(18):** 3865–3868.

[24] DELLY B. Hardness conserving semilocal pseudopotentials. *Phys. Rev. B*, 2002, **66(15):** 155125.

[25] TODOROVA T, DELLY B. Wetting of paracetamol surfaces studied by $DMol^3$-COSMO calculations. *Mol. Simulat.*, 2008, **34(10/15):** 1013–1017.

[26] WEI Z X, ZHANG Y F, WANG S Y, *et al*. Fe-doped phosphorene for the nitrogen reduction reaction. *J. Mater. Chem. A*, **6(28):** 13790–13796.

[27] SHI L, LI Q, LING C Y, *et al*. Metal-free electrocatalyst for reducing nitrogen to ammonia using a Lewis acid pair. *J. Mater. Chem. A*, 2019, **7(9):** 4865–4871.

[28] JIANG C H, ZHOU R Q, PENG Z H, *et al*. An atomically thin layer of Ru/MoS_2 heterostructure: structural, electronic, and magnetic properties. *Phys. Chem. Chem. Phys.*, 2016, **18(47):** 32528–32533.

[29] YU X M, HAN P, WEI Z X, *et al*. Boron-doped graphene for electrocatalytic N_2 reduction. *Joule*, 2018, **2(8):** 1610–1622.

[30] NORSKOV J K, ROSSMEISL J, LOGADOTTIR A, *et al*. Origin of the overpotential for oxygen reduction at a fuel-cell cathode. *J. Phys. Chem. B*, 2004, **108(46):** 17886–17892.

[31] YANG L, FENG S, ZHU W, Tuning nitrate electroreduction activity *via* an equilibrium adsorption strategy: a computational study. *J Phys. Chem. Lett.*, 2022, **13(7):** 1726–1733.

[32] LIM D H, WILCOX J. Mechanisms of the oxygen reduction reaction on defective graphene-supported Pt nanoparticles from first-principles. *J. Phys. Chem. C*, 2012, **116(5):** 3653–3660.

[33] YIN J, FANG Q H, LI Y X, *et al*. Ni-C-N nanosheets as catalyst for hydrogen evolution reaction. *J. Am. Chem. Soc.*, 2016, **138(44):** 14546–14549.

[34] LIANG H W, BRULLER S, DONG R H, *et al*. Molecular metal-N_x centres in porous carbon for electrocatalytic hydrogen evolution. *Nat. Commun.*, 2015, **6(1):** 7992.

[35] LING C Y, OUYANG Y X, LI Q, *et al*. A general two-step strategy-based high-throughput screening of single atom catalysts for nitrogen fixation. *Small Methods*, 2019, **3(9):** 1–8.

[36] QI J M, GAO L Y, WEI F F, *et al*. Design of a high-performance electrocatalyst for N_2 conversion to NH_3 by trapping single metal atoms on stepped CeO_2. *ACS Appl. Mater. Interfaces*, 2019, **11(50):** 47525–47534.

[37] SKULASON E, BLIFAARD T, GUDMUNDSDOTTIR S. A theoretical evaluation of possible transition metal electro-catalysts for N_2 reduction. *Phys. Chem. Chem. Phys.*, 2012, **14(3):** 1235–1245.

[38] CHOI W I, WOOD B C, SCHWEGLER E, *et al*. Combinatorial search for high-activity hydrogen catalysts based on transition-metal-embedded graphitic carbons. *Adv. Energy Mater.*, 2015, **5(23):** 1501423.

[39] LIU C W, LI Q Y, ZHANG J, *et al*. Conversion of dinitrogen to ammonia on Ru atoms supported on boron sheets: a DFT study. *J. Mater. Chem. A*, 2019, **7(9):** 4771–4776.

[40] LI X F, LI Q K, CHENG J, *et al*. Conversion of dinitrogen to ammonia by FeN_3-embedded graphene. *J. Am. Chem. Soc.*, 2016, **138(28):** 8706–8709.

[41] QIU W B, XIE X Y, QIU J D, *et al*. High-performance artificial nitrogen fixation at ambient conditions using a metal-free electrocatalyst. *Nat. Commun.*, 2018, **9(1):** 3485.

[42] GUO Y, GU J X, ZHANG R, *et al*. Molecular crowding effect in aqueous electrolytes to suppress hydrogen reduction reaction and enhance electrochemical nitrogen reduction. *Adv. Energy Mater*., 2021, **11(36):** 2101699.

[43] GUO Y X, YAO Z Y, TIMMER B J J, *et al*. Boosting nitrogen reduction reaction by bio-inspired FeMoS containing hybrid electrocatalyst over a wide pH range. *Nano Energy*, 2019, **62:** 282–288.

[44] WANG X, FENG Z, XIAO B, *et al*. Polyoxometalate-based metal-organic framework-derived bimetallic hybrid materials for upgraded electrochemical reduction of nitrogen. *Green Chem*., 2020, **22(18):** 6157–6169.

[45] ZHAO J X, CHEN Z F. Single Mo atom supported on defective boron nitride monolayer as an efficient electrocatalyst for nitrogen fixation: a computational study. *J. Am. Chem. Soc.*, 2017, **139(36):** 12480–12487.

[46] LING C Y, BAI X W, OUYANG Y X, *et al*. Single molybdenum atom anchored on N-doped carbon as a promising electrocatalyst for nitrogen reduction into ammonia at ambient conditions. *J. Phys. Chem. C*, 2018, **122(29):** 16842–16847.

[47] WU Y B, HE C, ZHANG W X, "Capture-backdonation-recapture" mechanism for promoting N_2 reduction by heteronuclear metal-free double-atom catalysts. *J Am. Chem. Soc.* 2022, **144(21):** 9344–9353.

NiN_4/Cr 修饰的石墨烯电化学固氮电极

吴 静[1], 余立兵[1], 刘帅帅[1], 黄秋艳[1], 姜姗姗[1],
ANTON Matveev[2], 王连莉[3], 宋二红[4], 肖蓓蓓[1]

(1. 江苏科技大学 能源与动力学院, 镇江 212003; 2. 莫尔多瓦州立大学, 萨兰斯克 430005, 俄罗斯; 3. 西安科技大学 材料科学与工程学院, 西安 710054; 4. 中国科学院 上海硅酸盐研究所, 高性能陶瓷和超微结构国家重点实验室, 上海 200050)

摘 要: 工业上应用哈伯工艺法合成氨过程要求严苛, 需要消耗大量能源且二氧化碳排放量大。因此, 开发在常规环境条件下通过电催化氮还原反应的清洁技术, 对未来可持续的能源转化进程具有重要意义。本研究采用密度泛函理论计算方法, 对 TM_1N_4/TM_2 嵌入石墨烯的氮还原反应进行了全面研究。在充分考虑活性和稳定性的情况下, 研究结果表明, NiN_4/Cr 锚定石墨烯通过酶促反应途径表现出最佳的催化活性, 其中第一次加氢为电位决定步骤, 起始电位为 0.57 V, 优于商业 Ru 基材料。此外, 与单一的 Cr 原子修饰的石墨烯相比, 引入 NiN_4 官能团降低了 ΔG_{max} 并提高了电催化性能。根据 Mulliken 电荷分析, 催化剂的催化活性主要来源于载体和反应中间体之间的电子转移。上述结果为高效合成氨提供了电极候选材料, 进一步深化了相应的电催化机理。

关 键 词: 氮气还原反应; 石墨烯; 密度泛函原理; 电催化; 热力学

中图分类号: TQ174 **文献标志码**: A

Supporting Materials:

NiN_4/Cr Embedded Graphene for Electrochemical Nitrogen Fixation

WU Jing[1], YU Libing[1], LIU Shuaishuai[1], HUANG Qiuyan[1], JIANG Shanshan[1], Anton Matveev[2], WANG Lianli[3], SONG Erhong[4], XIAO Beibei[1]

(1. School of Energy and Power Engineering, Jiangsu University of Science and Technology, Zhenjiang 212003, China; 2. National Research Ogarev Mordovia State University, Saransk 430005, Russia; 3. School of Materials Science and Engineering, Xi'an University of Science and Technology, Xi'an 710054, China; 4. The State Key Laboratory of High Performance Ceramics and Superfine Microstructure, Shanghai Institute of Ceramics, Chinese Academy of Sciences, Shanghai 200050, China)

Table S1　Adsorption energies E_{ads} on Mn_1N_4/TM_2 (E_{ads} in eV)

3d	Sc	Ti	V	Cr	Mn	Fe	Co	Ni
$E_{ads}(TM_2)$ N_2 end-on	–0.22	–0.36	–0.62	–0.72	–1.02	–1.07	–0.89	–0.59
$E_{ads}(TM_2)$ N_2 side-on	0.12	–0.02	–1.17	–0.35	–0.59	–0.51	–0.33	–0.19
$E_{ads}(TM_2)$ H	0.75	0.20	–0.18	–0.14	–0.19	–0.20	–0.22	–0.38
4d	Y	Zr	Nb	Mo	Tc	Ru	Rh	Pd
$E_{ads}(TM_2)$ N_2 end-on	–0.14	–0.22	–1.05	–0.70	–0.73	–0.99	–0.73	–1.30
$E_{ads}(TM_2)$ N_2 side-on	–0.13	0.11	–0.42	–0.43	–0.47	–0.44	–0.25	–0.96
$E_{ads}(TM_2)$ H	0.78	0.25	–0.87	–0.38	0.51	–0.11	–0.33	–1.06
5d	Lu	Hf	Ta	W	Re	Os	Ir	Pt
$E_{ads}(TM_2)$ N_2 end-on	–0.21	–0.35	–0.60	–1.57	–1.23	–1.30	–1.08	–0.52
$E_{ads}(TM_2)$ N_2 side-on	0.07	0.02	–0.32	–1.48	–0.88	–0.68	–0.44	–0.23
$E_{ads}(TM_2)$ H	0.65	–0.01	–1.33	–0.92	–0.88	–0.81	–0.87	–0.99

Table S2　Adsorption energies E_{ads} on Fe_1N_4/TM_2 (E_{ads} in eV)

3d	Sc	Ti	V	Cr	Mn	Fe	Co	Ni
$E_{ads}(TM_2)$ N_2 end-on	–0.21	–0.75	–0.26	–0.52	–0.94	–1.06	–0.88	–0.53
$E_{ads}(TM_2)$ N_2 side-on	–0.21	–0.37	–0.35	–0.41	–0.59	–0.54	–0.25	–0.56
$E_{ads}(TM_2)$ H	0.93	0.33	0.27	–0.02	–0.14	–0.25	–0.11	–0.37
4d	Y	Zr	Nb	Mo	Tc	Ru	Rh	Pd
$E_{ads}(TM_2)$ N_2 end-on	–0.14	–0.22	–0.20	–0.62	–0.88	–0.96	–0.76	–0.49
$E_{ads}(TM_2)$ N_2 side-on	0.22	–0.20	–0.20	0.01	–0.58	–0.41	–0.27	0.01
$E_{ads}(TM_2)$ H	0.90	0.21	0.17	–0.23	–0.12	–0.12	–0.09	–0.33
5d	Lu	Hf	Ta	W	Re	Os	Ir	Pt
$E_{ads}(TM_2)$ N_2 end-on	–0.20	–0.31	–0.64	–0.91	–1.15	–1.27	–1.09	–0.26
$E_{ads}(TM_2)$ N_2 side-on	–0.20	0.07	–0.49	–0.77	–0.94	–0.68	–0.48	0.22
$E_{ads}(TM_2)$ H	0.77	0.01	–0.73	–0.84	–0.68	–0.78	–0.72	–0.99

Table S3 Adsorption energies E_{ads} on Co_1N_4/TM_2 (E_{ads} in eV)

3d	Sc	Ti	V	Cr	Mn	Fe	Co	Ni
$E_{ads}(TM_2)$ N_2 end-on	–0.21	–0.37	–0.68	–0.84	–1.01	–1.05	–0.85	–0.46
$E_{ads}(TM_2)$ N_2 side-on	–0.20	–0.37	–0.29	–0.51	–0.64	–0.53	–0.26	–0.56
$E_{ads}(TM_2)$ H	1.02	0.37	–0.09	–0.08	–0.36	–0.13	–0.07	–0.28
4d	Y	Zr	Nb	Mo	Tc	Ru	Rh	Pd
$E_{ads}(TM_2)$ N_2 end-on	–0.12	–0.19	–0.44	–0.61	–0.82	–0.93	–0.75	–0.48
$E_{ads}(TM_2)$ N_2 side-on	–0.13	–0.20	–0.03	–0.29	–0.57	–0.42	–0.25	–0.48
$E_{ads}(TM_2)$ H	1.03	0.42	–0.12	–0.22	–0.07	–0.07	–0.03	–0.26
5d	Lu	Hf	Ta	W	Re	Os	Ir	Pt
$E_{ads}(TM_2)$ N_2 end-on	–0.20	–0.29	–0.62	–0.86	–1.08	–1.23	–1.07	–0.49
$E_{ads}(TM_2)$ N_2 side-on	–0.21	–0.29	–0.28	–0.63	–0.89	–0.67	–0.46	–0.48
$E_{ads}(TM_2)$ H	0.82	0.23	–0.50	–0.75	–0.63	–0.72	–0.69	–0.87

Table S4 Adsorption energies E_{ads} on Ni_1N_4/TM_2 (E_{ads} in eV)

3d	Sc	Ti	V	Cr	Mn	Fe	Co	Ni
$E_{ads}(TM_2)$ N_2 end-on	–0.21	–0.41	–0.72	–0.91	–1.04	–1.07	–0.79	–0.58
$E_{ads}(TM_2)$ N_2 side-on	–0.19	0.02	–0.41	–0.63	–0.66	–0.50	/	–0.58
$E_{ads}(TM_2)$ H	0.97	0.19	–0.14	–0.40	–0.23	–0.22	–0.18	–0.27
4d	Y	Zr	Nb	Mo	Tc	Ru	Rh	Pd
$E_{ads}(TM_2)$ N_2 end-on	–0.12	–0.24	–0.51	–0.70	–0.91	–0.98	–0.73	–0.48
$E_{ads}(TM_2)$ N_2 side-on	–0.13	–0.20	–0.23	–0.63	–0.61	–0.44	–0.21	–0.48
$E_{ads}(TM_2)$ H	0.97	0.15	–0.33	–0.22	–0.12	–0.13	–0.16	–0.25
5d	Lu	Hf	Ta	W	Re	Os	Ir	Pt
$E_{ads}(TM_2)$ N_2 end-on	–0.20	–0.33	–0.74	–0.98	–1.17	–1.30	–1.06	–0.65
$E_{ads}(TM_2)$ N_2 side-on	–0.20	0.06	–0.49	–0.94	–0.95	–0.68	–0.41	–0.65
$E_{ads}(TM_2)$ H	0.85	0.02	–0.71	–0.66	–0.69	–0.82	–0.81	–0.93

Table S5 Free energy change ΔG (ΔG in eV), R_i stands for the i^{th} protonation step

System	Mechanisms	N_2 adsorption	R_1	R_2	R_3	R_4	R_5	R_6	NH_3 desorption
NiN_4/Cr	Distal	–0.41	0.98	–0.28	0.17	–1.08	–1.09	–0.23	1.04
	Alternating	–0.41	0.98	0.05	–0.31	–0.25	–1.29	–0.71	1.04
	Enzymatic	–0.10	0.57	0.16	–0.56	–0.12	–1.51	–0.38	1.04
NiN_4/Mo	Distal	–0.27	0.92	–0.08	–0.22	–1.14	–0.71	–0.20	1.04
	Alternating	–0.27	0.92	0.16	–0.56	0.06	–1.52	–0.49	1.04
	Enzymatic	–0.11	0.60	0.18	–0.89	0.50	–1.54	–0.44	1.04
NiN_4/Ta	Distal	–0.18	0.69	–0.37	–0.06	–1.22	–1.02	0.22	1.04
	Alternating	–0.18	0.69	0.05	–0.88	0.11	–1.78	0.05	1.04
	Enzymatic	0.04	0.11	–0.23	–0.70	0.58	–1.70	–0.04	1.04

Table S6 Potential determining step and its free energy change ΔG_{max}(ΔG_{max} in eV)

	Distal		Alternating		Enzymatic	
	RDS	ΔG_{max}	RDS	ΔG_{max}	RDS	ΔG_{max}
Cr	$*N_2+H\rightarrow*NNH$	1.03	$*N_2+H\rightarrow*NNH$	1.03	$*N*N+H\rightarrow*N*NH$	0.66
NiN_4/Cr	$*N_2+H\rightarrow*NNH$	0.98	$*N_2+H\rightarrow*NNH$	0.98	$*N*N+H\rightarrow*N*NH$	0.57
Mo	$*N_2+H\rightarrow*NNH$	1.27	$*N_2+H\rightarrow*NNH$	1.27	$*N*N+H\rightarrow*N*NH$	0.43
NiN_4/Mo	$*N_2+H\rightarrow*NNH$	0.92	$*N_2+H\rightarrow*NNH$	0.92	$*N*N+H\rightarrow*N*NH$	0.60
Ta	$*NNH_2+H\rightarrow*N$	0.72	$*N_2+H\rightarrow*NNH$	0.66	$*NH*NH_2+H\rightarrow*NH_2*NH_2$	0.49
NiN_4/Ta	$*N_2+H\rightarrow*NNH$	0.69	$*N_2+H\rightarrow*NNH$	0.69	$*NH*NH_2+H\rightarrow*NH_2*NH_2$	0.58

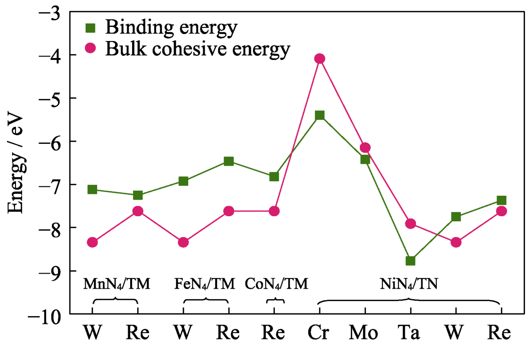

Fig. S1 Comparison of binding energy and bulk cohesive energy of the selected complexes

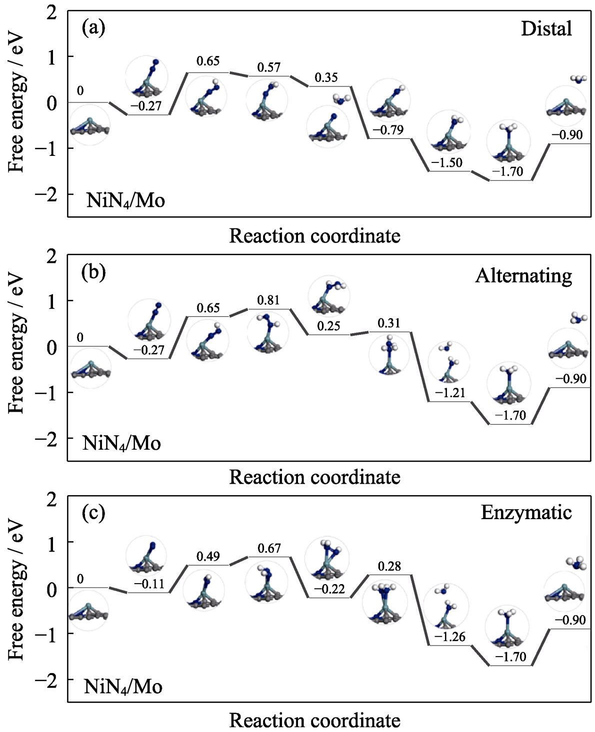

Fig. S2 Free energy diagrams and the corresponding configuration of the NRR intermediates on NiN_4/Mo

NRR mechanisms are (a) distal, (b) alternating, and (c) enzymatic, respectively

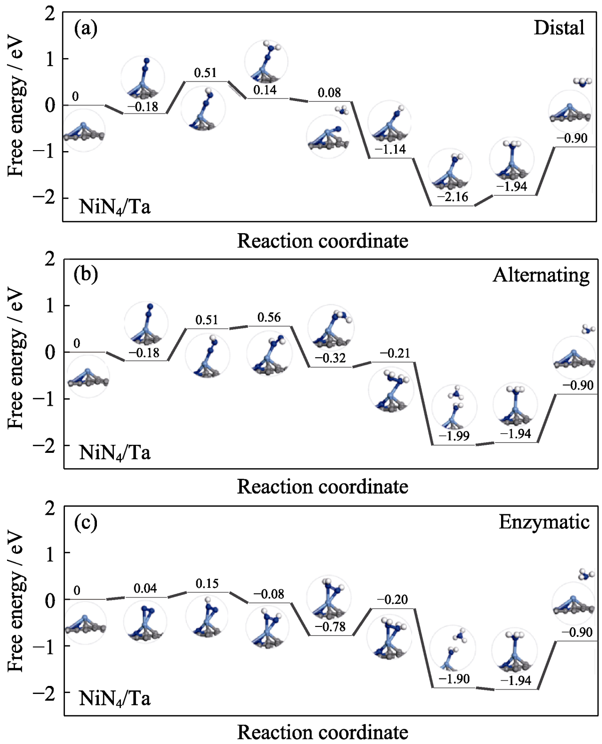

Fig. S3 Free energy diagrams and the corresponding configuration of the NRR intermediates on NiN_4/Ta

NRR mechanisms are (a) distal, (b) alternating, and (c) enzymatic, respectively

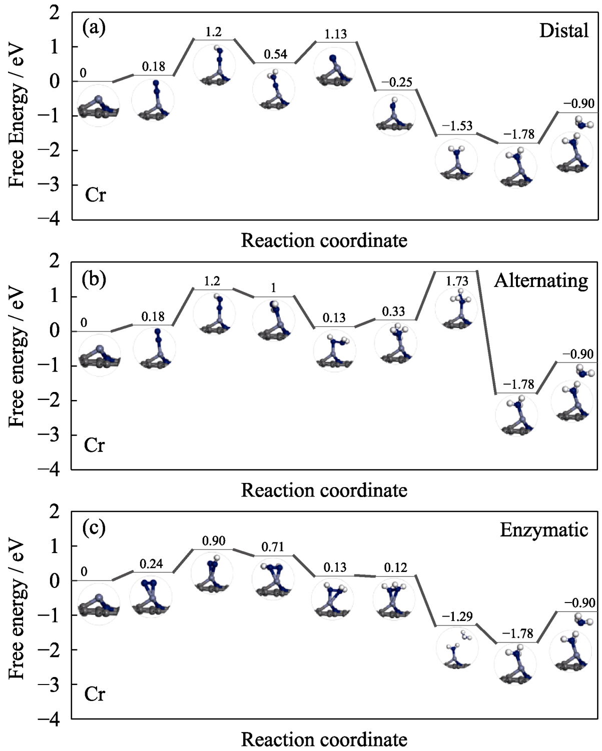

Fig. S4 Free energy diagrams and the corresponding configuration of the NRR intermediates on Cr embedded nitrogen functionalized graphene

NRR mechanisms are (a) distal, (b) alternating, and (c) enzymatic, respectively

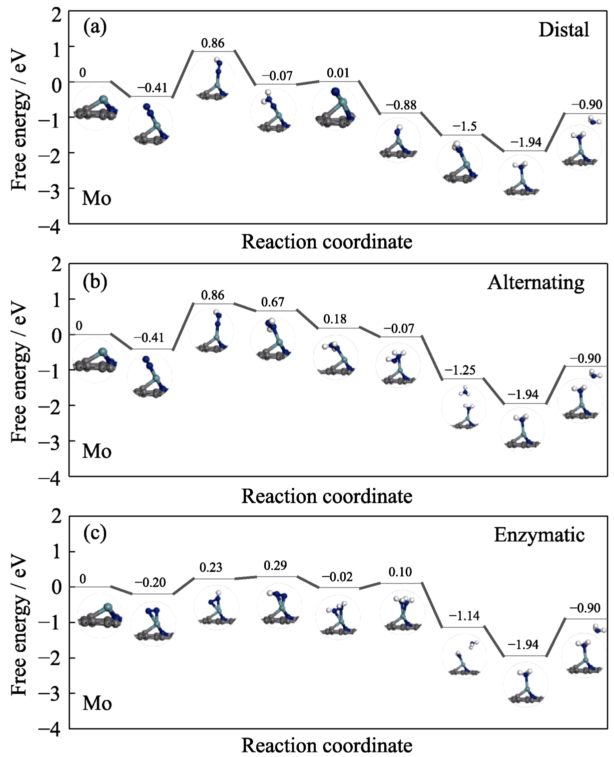

Fig. S5　Free energy diagrams and the corresponding configuration of the NRR intermediates on Mo embedded nitrogen functionalized graphene

NRR mechanisms are (a) distal, (b) alternating, and (c) enzymatic, respectively

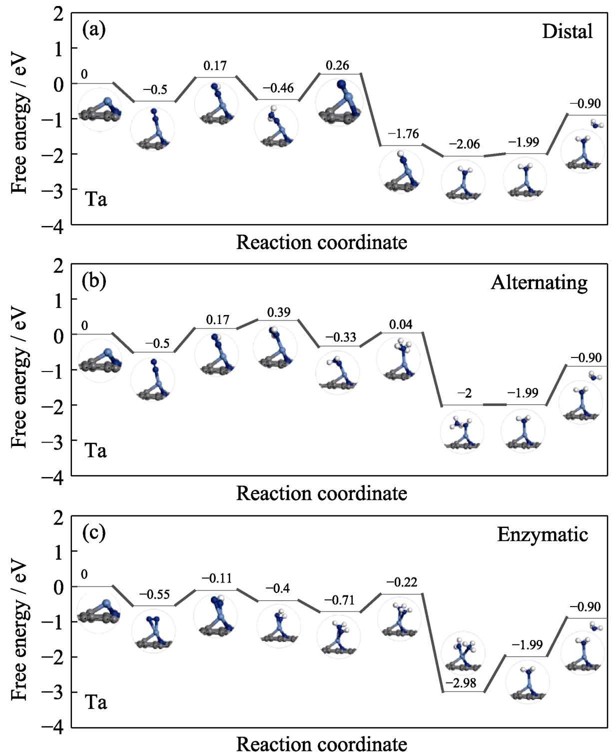

Fig. S6　Free energy diagrams and the corresponding configuration of the NRR intermediates on Ta embedded nitrogen functionalized graphene

NRR mechanisms are (a) distal, (b) alternating, and (c) enzymatic, respectively

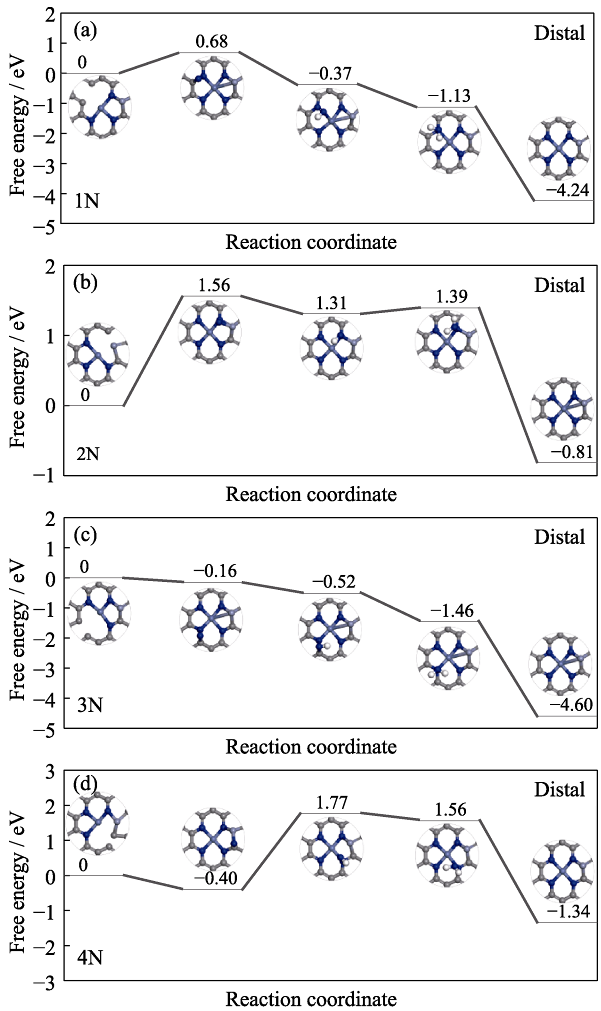

Fig. S7　Free energy profiles of N_2-to-NH_3 conversion on the N vacancy

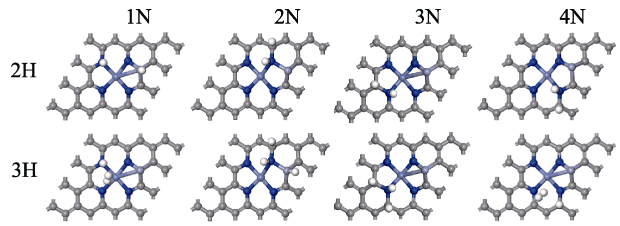

Fig. S8　Atomic configurations of the hydrogen adsorption on the nitrogen embedded in graphene after geometry optimization